Materials and Design 198 (2021) 109313

Contents lists available at ScienceDirect

Materials and Design

journal homepage: www.elsevier.com/locate/matdes

A mathematically defined 3D auxetic metamaterial with tunable mechanical and conduction properties

Xiaoyang Zheng [a,b], Xiaofeng Guo [c], Ikumu Watanabe [a,b,*]

[a] Graduate School of Pure and Applied Sciences, University of Tsukuba, 1-1-1 Tennodai, Tsukuba 305-8573, Japan
[b] Research Center for Structural Materials, National Institute for Materials Science, 1-2-1 Sengen, Tsukuba 305-0047, Japan
[c] School of Materials Science and Engineering, Southwest University of Science and Technology, Mianyang 621010, China

HIGHLIGHTS

- We propose a novel 3D auxetic metamaterial derived from a mathematically defined triply periodic minimal surface.
- Nickel plating enhanced the stiffness, strength, and conductivity of the metamaterial without the auxeticity and resilience.
- The relationships between geometric parameters and material properties of the metamaterial were discussed.
- These relationships provide insight into tuning its performance over a broad range.

GRAPHICAL ABSTRACT

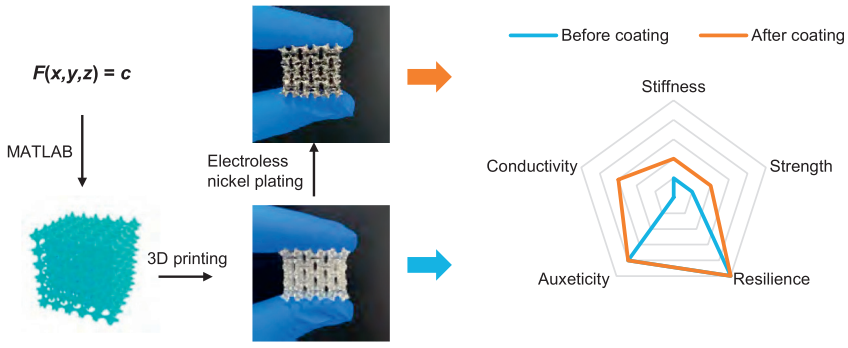

ARTICLE INFO

Article history:
Received 20 September 2020
Received in revised form 4 November 2020
Accepted 8 November 2020
Available online 17 November 2020

Keywords:
Negative Poisson's ratio
Metamaterial
Minimal surface
3D printing
Electroless plating

ABSTRACT

An auxetic metamaterial is a type of mechanical metamaterial that has a negative Poisson's ratio. Most auxetic metamaterials are truss-based or originate from Boolean operations of simple geometries. Herein, we introduce a new 3D auxetic metamaterial that is mathematically generated from an implicit expression. Further, this metamaterial is fabricated by 3D printing using a flexible material, which allows it to recover from large deformations. The buckling-induced auxetic behavior of the metamaterial was first evaluated via compression tests and finite element analyses. A nickel layer was then plated onto the surface to enhance its stiffness, strength, and conductivity without loss of auxeticity and resilience. The integration of 3D printing and electroless plating enabled accurate control over the mechanical and conduction properties of the auxetic metamaterial; these properties are presented as contour maps for guidance in functional applications.
© 2020 The Authors. Published by Elsevier Ltd. This is an open access article under the CC BY-NC-ND license (http://creativecommons.org/licenses/by-nc-nd/4.0/).

1. Introduction

Auxetic metamaterials constitute a class of mechanical metamaterials that have topology-controlled properties. They have attracted widespread attention because of their inherently unique mechanical performance in terms of their negative Poisson's ratio [1–4]. When auxetic metamaterials are uniaxially compressed, they contract in all directions, whereas common structural materials, such as polymers and polycrystalline metals, whose Poisson's ratios are generally in the range of 0.25–0.35, expand in a direction perpendicular to the applied load. Further, when bent, a plate made of an auxetic metamaterial deforms into a convex shape, whereas a plate made of a material with a positive Poisson's ratio deforms into a saddle shape. Because of specific characteristics such as synclastic behavior, shear resistance, fracture

* Corresponding author at: Graduate School of Pure and Applied Sciences, University of Tsukuba, 1-1-1 Tennodai, Tsukuba 305-8573, Japan.
E-mail address: WATANABE.Ikumu@nims.go.jp (I. Watanabe).

https://doi.org/10.1016/j.matdes.2020.109313
0264-1275/© 2020 The Authors. Published by Elsevier Ltd. This is an open access article under the CC BY-NC-ND license (http://creativecommons.org/licenses/by-nc-nd/4.0/).

resistance, indentation resistance, and variable permeability, they are considered as promising candidates in strain sensing [5,6], actuation [7,8], biomedicine [9,10], aerospace applications [11,12], and electrochemical energy storage and conversion [13–15]. Consequently, considerable efforts have been devoted to the development and fabrication of new auxetic metamaterials.

Auxetic metamaterials are typically classified into re-entrant [16–23], chiral [24–28], rotating [29–34], and hierarchical laminate structures [35–37] according to their deformation mechanisms. In general, the re-entrant, chiral, and rotating structures are porous and composed of a single component, whereas the hierarchical laminate structures are solid and consist of two or more components with different Poisson's ratios. The empty spaces in the interior structures of these materials are necessary for rotation, bending, and torsion of the ligaments and nodes in the former three analogies, resulting in low stiffnesses and strengths compared with their matrix materials. Most auxetic metamaterials have periodic array structures according to their design principles in terms of the components, porosities, and periodicities. These basic arrays generally comprise beams, trusses, or shells, or are generated from Boolean operations of simple geometries, such as cylinders, cones, spheres, and boxes (Fig. 1). The modeling method greatly limits its applications, especially where optimal performances are needed.

However, triply periodic minimal surfaces (TPMSs), which are a type of metamaterial, have recently gained much attention owing to their mathematically controlled and fascinating topologies [38,39], such as their bioinspired morphology, smooth surfaces without edges and corners [40], and higher stiffness and strength than their disordered counterparts [41]. Extensive efforts have been invested to expand the design spaces of TPMS-based materials, such as skeletal, sheet, graded, and hybrid lattice structures [42–46]; however, thus far, only a few studies have focused on achieving negative Poisson's ratios [47,48]. Herein, we extend the application of TPMSs to auxetic metamaterials by exploiting their particular characteristics.

3D printing or additive manufacturing is a standard method used to fabricate delicately designed auxetic metamaterials. Rubber-like materials, such as flexible resins and thermoplastic polyurethane, are the typical raw materials used for 3D-printed auxetic metamaterials, which render them resilient but result in inadequate stiffness and strength [49–51]. Metal-based 3D printing techniques allow the fabrication of auxetic metamaterials made of metals, such as structural steel and titanium alloy [52,53]; however, the plasticity highly restricts their application where large deformations are required. Although some fabrication methods have been developed to ensure both resilience and stiffness, the feasible structures are highly limited. For instance, wire-woven metals manufactured by forming helical wires can achieve high energy absorption and fracture resistance capabilities. However, their basic geometries are mainly 3D truss-like cells, which do not allow fabricating complex internal shapes [34,54].

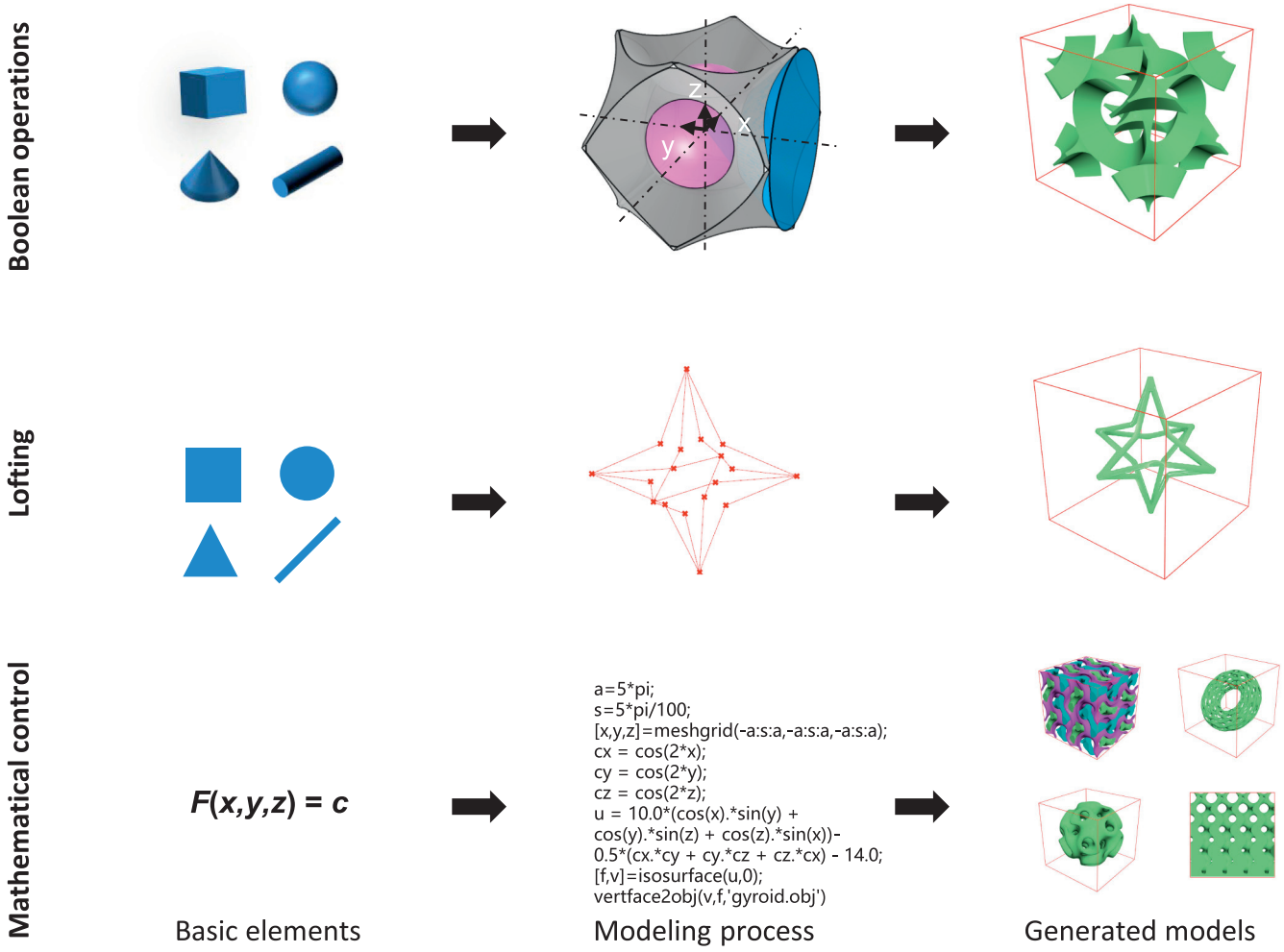

Fig. 1. Three common methods used to generate auxetic metamaterials: Boolean operations, lofting, and mathematical control. Mathematical control is used in this work and could generate serveral complicated structures based on implicit expressions.

In the present work, we combine 3D printing with electroless plating to derive a new type of auxetic metamaterial from TPMSs. First, the geometries of the TPMS-based auxetic metamaterial are mathematically generated with an arbitrary relative density. We then investigate the auxetic behavior of the metamaterial under uniaxial compression using a 3D-printed specimen, followed by verification via finite element method (FEM) simulations. Next, we metalize the 3D-printed models by plating a layer of nickel on their surfaces and evaluate their performance under multiple compression tests. Finally, we quantify the effective mechanical and conduction properties and present them in the form of maps depending on the relative densities and nickel layer thicknesses.

2. Methods

2.1. Generation of microstructures

A minimal surface is a smooth surface that has zero mean curvature and locally minimizes the surface area for a given boundary [55]. When a minimal surface is translationally symmetric in three dimensions, it is called a TPMS. TPMSs can be modeled using different level-set approximation equations. In this work, the geometry of the auxetic metamaterial is derived from Schwarz Primitive minimal surface [56], and a more complicated implicit equation is used to determine the isosurface of the designed structure [46]:

$$F(x,y,z) = (\cos(x) + \cos(y) + \cos(z)) - 0.4(\cos(x)\cos(y) + \cos(y)\cos(z) + \cos(z)\cos(x)) + c \quad (1)$$

Here, the level-set constant c regulates the volume fractions of the two phases separated by the isosurface. A skeletal lattice is built after capping the open borders of the isosurface. The proposed auxetic metamaterial possesses a cubic symmetry with a single unit cell within the domain x, y, $z \in [-\pi,\pi]$. Its relative density, denoted by ρ (i.e., the volume fraction of the solid phase), has an almost linear relationship with c, as shown in Fig. 2a. In this work, each isosurface was generated on the basis of the implicit expression using MATLAB (MathWorks, USA). After capping the isosurface borders, the geometry of the TPMS-based auxetic metamaterial was exported as standard triangle language (.STL) files for 3D printing and FEM simulations. Fig. 1 compares three different methods used to generate auxetic metamaterials: Boolean operations of simple geometries, lofting operations that create 3D objects using 3D lattices as framework with arbitrary cross-sectional shapes such as cycle and square, and mathematical control. It demonstrates the flexibility of mathematical control to build complicated structures based on TPMS-based unit cells.

2.2. Specimen preparation

To reduce the effects of the dimensions on the experiments, each model used in the experiments consisted of 6 × 6 × 6 unit cells (Fig. 2b). The specimens of the proposed auxetic metamaterial were fabricated using an elastic photopolymer resin (Elastic 50A resin, Formlabs, USA) and a 3D printer (Form 3, Formlabs, USA). To achieve a subtle surface finish, no additional support structures were used, and the layer thickness and length of each specimen were set to 0.05 mm and 24 mm, respectively. After washing with isopropanol for 10 min, these 3D-printed specimens were fully cured at 60 °C for 20 min.

We used an electroless nickel plating method to metalize the 3D-printed specimens. First, each sample was neutrally degreased in a cleaning solution containing 50 g/L Na_2CO_3, 35 g/L Na_2SiO_3, and 3 g/L $C_{12}H_{25}NaO_4S$ for 5 min. After rinsing thoroughly with distilled water for 2 min, the sample was etched in a 3 M NaOH solution for 30 min, followed by rinsing again with distilled water for 2 min. In the next stage, the sample was sensitized in an aqueous solution containing 20 g/L $SnCl_2$ and 20 mL/L 37% HCl for 5 min, and thereafter activated in an aqueous solution containing 0.1 g/L $PdCl_2$ and 20 mL/L 37% HCl for 5 min. After rinsing with distilled water, nickel was deposited in an electroless manner using a nickel plating bath containing 32 g/L $NiSO_4{\cdot}6(H_2O)$, 20 g/L $Na_3C_6H_5O_7$, 25 g/L NH_4Cl, and 28 g/L $NaPO_2H_2$. This step was performed at 90 °C, and the plating time was varied from 5 to 30 min to achieve different nickel layer thicknesses. Finally, the nickel-coated sample was rinsed with distilled water and dried under a nitrogen stream. All chemicals used in the electroless nickel plating process were purchased from Sigma-Aldrich.

2.3. Characterization

Optical microscope images were obtained using a 3D digital microscope (DSX1000, OLYMPUS, Japan). Scanning electron micrographs

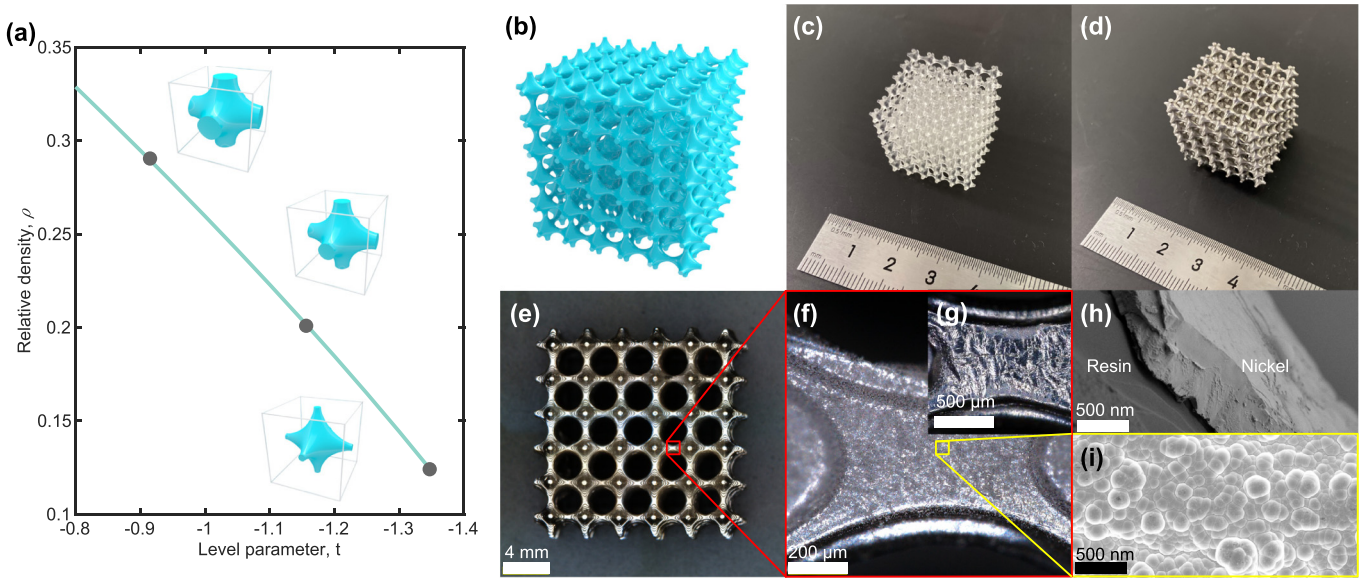

Fig. 2. TPMS-based auxetic metamaterial. (a) Different relative densities determined by the level-set constant c. (b) A rendering of the auxetic metamaterial consisting of 6 × 6 × 6 unit cells. (c,d) 3D-printed specimen before and after electroless nickel plating. (e,f) Optical microscope images of the nickel-coated specimen. (g) Optical microscope images of the nickel-coated specimen after multicle compression cycling. (h,i) Scanning electron micrographs showing the cross-sectional and surface morphologies of the nickel-coated specimen.

were acquired using a scanning electron microscope (Gemini500, Zeiss, UK) with an 8 mm working distance and 5 kV accelerating voltage. The surface of nickel layer was captured under Inlens detection signal, whereas the cross-section the nickel layer and the interface of the nickel layer and resin were captured under SE2 detection signal. The nickel thickness was determined by measuring the width of the nickel layers in the SEM images.

2.4. Uniaxial compression tests and current-voltage characteristics

The mechanical properties of the prepared specimens were evaluated by static compression tests using a motorized test stand (ESM303, Mark-10, USA). The specimens were uniaxially compressed between two plates at a constant displacement rate of 1 mm/min for both loading and unloading. These results were independent of the displacement rate, which is an excellent approximation to the stationary conditions in FEM simulations. The load and displacement data were recorded to produce stress-strain curves, and the deformation patterns of the specimens were captured using two cameras. With regard to the data analyses, the Poisson's ratios of each specimen were evaluated by extracting the displacements of the nodes of the deformed geometries from the recorded videos via postprocessing in MATLAB. The Young's moduli were measured by linearly fitting the initial linear portions of the stress-strain curves during loading. The critical buckling strains and stresses were defined by the 0.2% offset strain based on the shape of the stress-strain curves during loading.

The conduction properties of the specimens were also evaluated during the compression tests, as illustrated schematically in Fig. 3. The two compression plates were covered with insulating tape on the inside and copper foil tape on the outside. The copper foil tapes were connected to a digital sourcemeter (Series 2400 SourceMeter SMU, Keithley, USA) to determine the current-voltage characteristics. A constant voltage (U) of 0.2 V was applied to obtain the electric currents (I) under different strains. Thus, the electrical conductivity (κ) is determined by the equation $\kappa = IL/UL_0{}^2$, where L is the height of the 3D-printed models during the compression, $L_0 = 24$ mm that is the length of the 3D-printed models, and $S = L_0{}^2$ that is the sectional area of the 3D-printed models.

2.5. Finite element method simulations

The deformation behavior of the new auxetic metamaterial were further quantitatively investigated using an FEM simulation platform (COMSOL Multiphysics Ver. 5.4, COMSOL, Sweden). As the 3D-printed resin can be considered as a hyperelastic material, we defined the matrix material in the simulations using the incompressible neoHookean model for simplicity. The material model was a single parameter model with a Young's modulus of 0.6615 MPa that was fitted from the compression tests. As the deformation behavior under compression was subject to buckling instability, a linearized buckling analysis was first performed to compute the first-order buckling mode shape, followed by a post-buckling analysis using the computed mode shape. For the linearized buckling analysis, a fixed external load was applied along the z-axis to compute the shape of the buckling mode. For the post-buckling analysis, a parametric sweep of the displacement along the z-axis was used with a stop condition when adjacent boundaries were in contact. The post-buckling analysis helped to obtain the stress-strain curves in the three-dimensional Euclidean space. Specifically, models were built using approximately 2.5×10^5 second-order tetrahedral solid elements. All simulations were performed under periodic boundary conditions. The method applies these periodic boundary conditions to the three pairs of faces of the unit cell, which is based on a representative volume element (RVE) technique [57,58].

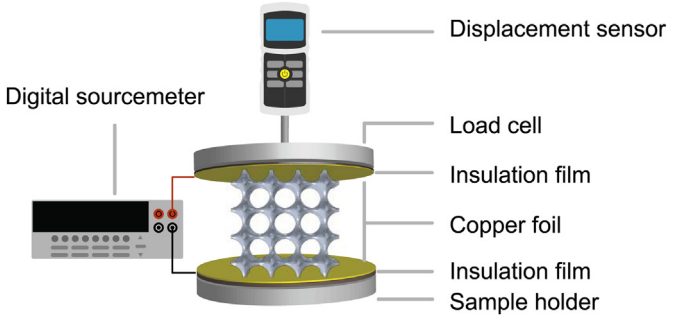

Fig. 3. Schematic illustrating the stressstrain and conductivitystrain curves by uniaxial compression tests.

3. Results and discussion

3.1. Auxetic behavior

The auxetic behavior and deformation mechanism of the newly fabricated metamaterial were investigated under uniaxial compression. As can be seen from the 3D visualization of the metamaterial (Fig. 2a), a single unit cell consists of three ligaments, which are orthogonal to the center node in 3D Euclidean space. This forms a single continuous lattice structure with smooth surfaces. We first conducted a uniaxial compression test on the 3D-printed specimen with $\rho = 0.16$ (Fig. 2c). The high resolution of the 3D printing technique ensured a good surface finish for the 3D-printed samples.

Then, we performed a systematical analysis of the auxetic behavior by considering the deformed patterns, strain-stress curves, and Poisson's ratios, as shown in Figs. 4 and 5. Fig. 4a shows a sequence of progressively deformed shapes of the specimen under seven different levels of longitudinal engineering strain (i.e., change in the height of the sample divided by its original height, $\varepsilon_{zz} = (L - L_0)/L_0$). Here, the specimen witnesses a dramatic contraction in all three directions, along with changes to its interior structure (the holes are changed from circles to ellipses). The lateral shrinkage proves that it is a 3D material with negative Poisson's ratio. The structural transformation from straight to bent ligaments demonstrates that the deformation behavior is subject to buckling instability. It is noted that the periodicity of the auxetic metamaterial can be considered as a new RVE comprising $2 \times 2 \times 2$ unit cells upon buckling.

To further probe the buckling-induced auxetic behavior, we analyzed the stresses and Poisson's ratios under different compression strains. Fig. 5a shows the stress-strain curve of the 3D-printed specimen as a function of the longitudinal strain ε_{zz}. It is observed that it is a typical elastic buckling curve consisting of a linear elastic regime and a stress plateau. The transition occurs at $\varepsilon_{zz} \approx -0.03$ when the ligaments begin to bend, which further demonstrates the buckling-induced auxetic behavior. Because the structure is difficult to shrink when there are no empty interior spaces, we set a stop condition when the ligaments around the holes come into mutual contact. As a result, the densification region of stress-strain curves is missed, and the overall deformation strain is approximately $\varepsilon_{zz} \approx -0.3$.

A more quantitative evaluation of the negative Poisson's ratios is shown in Fig. 5b, where these ratios are calculated from the engineering strain as $\nu_{ij} = -\varepsilon_{jj}/\varepsilon_{ii}$, for $i, j = x, y, z$. The transverse strains ε_{xx} and ε_{yy} are obtained from the average transverse strains of the four nodes of the inner-most RVE to reduce the influence of boundary conditions, including that of the friction on the up and down surfaces and the freedom of the exterior traction-free surfaces. This is attributable to the approximation that the innermost RVE can be assumed as an infinitely periodic structure [31]. The calculated Poisson's ratios (ν_{zx} and ν_{zy}) first monotonically decrease and then reach a plateau after $\varepsilon_{zz} \approx -0.1$. Each plateau lasts over a wide range from $\varepsilon_{zz} \approx -0.1$ to -0.3 for $\nu_{zx} \approx -0.5$ and $\nu_{zy} \approx -0.25$.

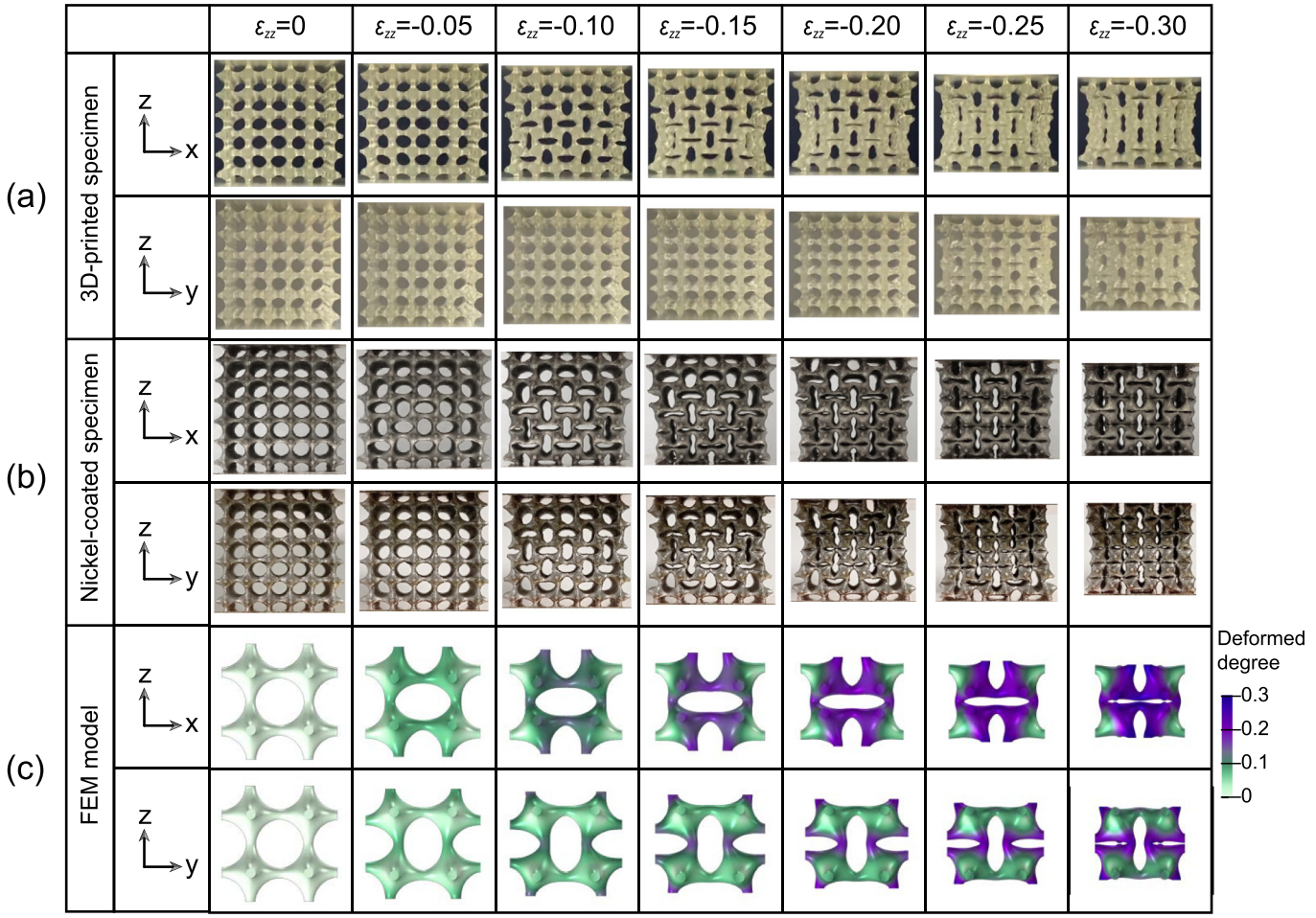

Fig. 4. Buckling-induced auxetic behavior of the proposed auxetic metamaterial and a sequence of progressively deformed configurations of the (a) 3D-printed specimen, (b) nickel-coated specimen, and (c) FEM model. The deformed degree is defined as the displacement norm of each meshed element divided by the original height of the model.

In the next stage, we conducted FEM simulations using an RVE consisting of 2 × 2 × 2 unit cells to investigate the auxetic behavior more qualitatively and quantitatively. The stress-strain curve of the FEM model shows excellent agreement with the result from the 3D-printed specimen (Fig. 5a). Moreover, the progressively deformed configurations from the FEM simulation are substantially alike compared to the experimental results (Fig. 4c). The geometry shrinks in all three directions accompanying the bending of ligaments and the rotation of nodes, demonstrating that the proposed auxetic metamaterial belongs to rotation structures. Fig. 5b presents the transverse strains ε_{xx} and ε_{yy} and the Poisson's ratios plotted as a function of the longitudinal strain ε_{zz}. It is clear that the transverse strains decrease with ε_{zz} under compression, exhibiting lateral constriction behavior. The Poisson's ratios calculated from the transverse strains also fit the experimental data well. The Poisson's ratios are positive during the initial compression and become negative after the structure undergoes buckling;

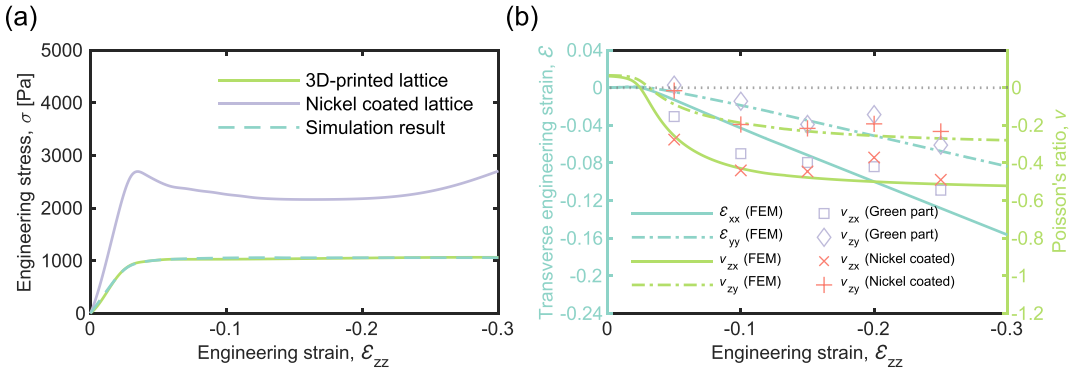

Fig. 5. (a) Stress-strain curves from uniaxial compression tests and FEM simulations. (b) Evolution of the transverse engineering strains and Poisson's ratios as a function of the longitudinal strain. The FEM results are observed to be in good agreement with the experimental data.

then, this trend gradually decreases and reaches a plateau with further loading. To clarify whether the periodic boundary condition will remove all possible size effects, we performed FEM simulations on a $6 \times 6 \times 6$ model using periodic boundary condition (Fig. 6). It shows the same result in terms of stressstrain curve, Young's modulus, and critical buckling stress and strain compared with the $2 \times 2 \times 2$ model. Further, Fig. 6 also reveals the deformation mechanism that leads to the auxetic effect; the compression leads to the bending of ligaments, the rotation of nodes, and the transformation of holes from circles to ellipses. Overall, the excellent agreement of the deformed patterns, stress-strain curves, and Poisson's ratios with the experimental observations demonstrate the accuracy and efficacy of our FEM model.

3.2. Influence of relative density

Given the outstanding qualitative and quantitative agreement between the experiment and the FEM simulation, we further explore the influence of the relative density of the new auxetic metamaterial on the mechanical properties based on FEM models. Five different relative densities ranging from 0.12 to 0.28 are considered. The stress-strain curves from the FEM simulation results are shown in Fig. 7a, where the stresses are normalized using the Young's modulus of the matrix material, $E_0 = 0.6615$ MPa. This shows that both the Young's modulus (E) and critical buckling stress (σ_c) increase with the relative density. The critical buckling strain (ε_c) also rises from about 0.009 to 0.101, providing evidence that a higher relative density suppresses the buckling behavior.

Fig. 7b presents the transverse strains ε_{xx} and ε_{yy} versus the longitudinal strain ε_{zz} from the FEM simulation results. The evolution of the transverse strains displays a similar tendency: a short plateau followed by a continuous decline. It is noteworthy that the short plateaus are extended, and the ultimate transverse strains are lessened as the relative density increases. We also calculated the Poisson's ratios from the transverse strains, as shown in Fig. 7c. Similarly, the Poisson's ratios at the same ε_{zz} increase with relative density, for example, the Poisson's ratios ν_{zx} increases from -0.58 to -0.29 at $\varepsilon_{zz} = -0.3$ when the relative density increases from 0.12 to 0.28. These results demonstrate that the proposed auxetic metamaterial is harder to shrink if it is denser. In addition, this auxetic metamaterial displays a transversely asymmetric behavior as $\nu_{zx} \neq \nu_{zy}$.

The performance of the proposed auxetic metamaterial, including Young's modulus, critical buckling strain and stress, and Poisson's ratio, is compared with several typical auxetic metamaterials, as shown in Fig. 8. The Young's moduli and critical stresses are normalized respectively by the Young's modulus of their constitute materials. It shows that the proposed auxetic metamaterial has higher normalized Young's modulus and critical stress than others owing to its higher relative density. Further, the structure possesses a longer buckling strain up to -0.1 at $\rho = 0.28$ and a larger negative Poisson's ratio up to -0.63 at $\rho = 0.12$. Overall, varying relative density enables to tune the mechanical properties over a broad range.

3.3. Influence of nickel layer

To further functionalize the auxetic metamaterial, we coated a conformal nickel layer onto the surfaces of the 3D-printed specimen with $\rho = 0.16$ by electroless plating. After plating a nickel layer of 0.57 μm thickness, the overall structure remains unchanged without apparent volume shrinkage or expansion (Fig. 2d). Moreover, the dense nickel layer, having a grain size of hundreds of nanometers, adheres to the resin surface well, thereby ensuring good structural stability after large deformation (Figs. 2e–i). Note that we assumed the relative density keeps unchanged after plating as the nickel layer thickness is quite small compared to the unit cell size of 3D-printed models.

Fig. 4b displays the continuous deformed patterns of the nickel-coated specimen under uniaxial compression, which exhibits a similar result as that of the 3D-printed specimen and FEM model. In addition, compared with the 3D-printed specimen, the nickel-coated specimen has nearly twice the values of the Young's modulus and critical buckling stress, but its critical buckling strain remains almost unchanged ($\varepsilon_c \approx -0.03$), as shown in Fig. 5a. Note that there are some decreases in the stresses after buckling owing to local plastic deformation and cracks in the nickel layers (Fig. 2g). Interestingly, the 3D-printed and nickel-coated specimens possess almost identical Poisson's ratios under the same transverse strains (Fig. 5b). The results prove that the nickel layer has a negligible impact on the critical buckling strain and Poisson's ratio, but significantly enhances its Young's modulus and critical buckling stress.

To investigate the resilience and stability of the specimens, we performed multicycle compression tests. Figs. 9a and b compare the 3D printed specimen with the nickel-coated specimen with respect to

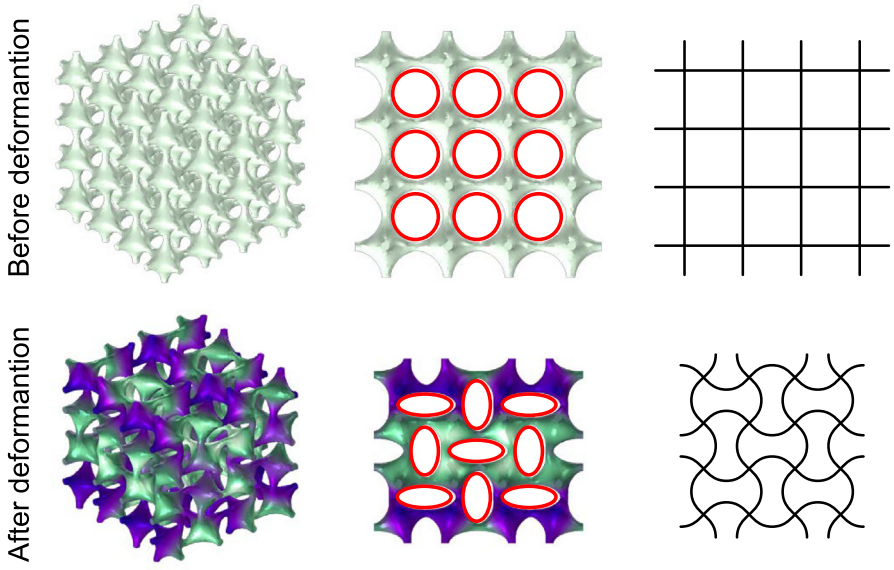

Fig. 6. Auxetic behavior of a $6 \times 6 \times 6$ model showing agreement with the $2 \times 2 \times 2$ model and revealing the deformation mechanism of the proposed auxetic metamaterial.

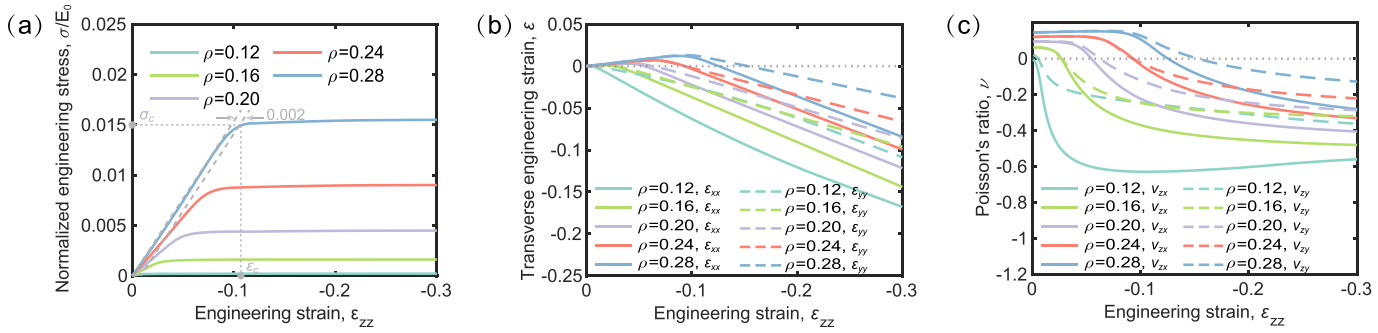

Fig. 7. Influence of relative density on mechanical properties. Evolutions of the (a) normalized engineering stresses, (b) transverse engineering strains, and (c) Poisson's ratios as function of the longitudinal strain. The methods of calculating Young's moduli E, critical buckling strains ε_c, and critical buckling stresses σ_c are also illustrated in the first figure.

their stress-strain curves during loading and unloading over multiple compression cycles. The small decreases in stresses for the nickel-coated specimen during consecutive compression cycles are a result of the local yield and crack of nickel layers. On the other hand, the Young's moduli decrease only marginally because the buckling behavior is a result of local deformation. When the load exceeds the critical buckling stress, the ligaments begin to bend, resulting in the plastic deformation and cracking of the nickel layers at the center of the ligaments where they bend. This part of the nickel layers contributes mainly to enhance the critical buckling stress. However, the Young's modulus is determined by entire nickel layer; the deformation and cracks of the nickel layers in these local regions reduce the Young's modulus only slightly. Nevertheless, both kinds of specimens reach peak stress when compressed to $\varepsilon_{zz} = -0.3$, and recover their original heights after load removal. The stress-strain curves are also nearly identical even after 20 compression cycles, demonstrating excellent resilience and stability for both classes of specimens.

To explore how the mechanical and conduction properties are enhanced by increasing the thickness of the nickel layers (t), we deposited nickel layers having different thicknesses on the 3D-printed specimens with $\rho = 0.16$ by varying the electroless plating time. The thicknesses of the nickel layers are nearly linearly dependent on the plating time, and a nickel layer of about 1.71 μm thickness was formed by plating 30 min (Fig. 9c). The stress-strain curves from the first cycle of compression tests are shown in Fig. 9d, revealing a mechanical enhancement that the stresses increase with the thickness at the same ε_{zz}. Compared with the non-plated specimen, the one with the 1.71 μm nickel layer has an approximately ten-fold increase in terms of its stiffness and strength, increasing from 35 kPa to 375 kPa in terms of Yongs modulus and from 0.9 kPa to 9 kPa in terms of critical buckling stress, respectively (Figs. 9e and f). Surprisingly, the critical buckling strains are almost independent of the thickness of the nickel layer, and have a constant value of $\varepsilon_{zz} \approx -0.03$.

After plating the nickel layer, these specimens become conductive. Fig. 10a displays the conductivity-strain curves of a sample with $t = 0.57$ μm and $\rho = 0.16$ during multiple compression tests. Likewise, the conductivity-strain curves also have excellent repeatability after 20 cycles of compression, without apparent losses in their conductivities. Under compression, the electrical conductivity increases linearly from 128 S/m initially to 230 S/m until the specimen suffers buckling; thereafter, it decreases immediately and then increases during further compression. After unloading, the electrical conductivity is almost

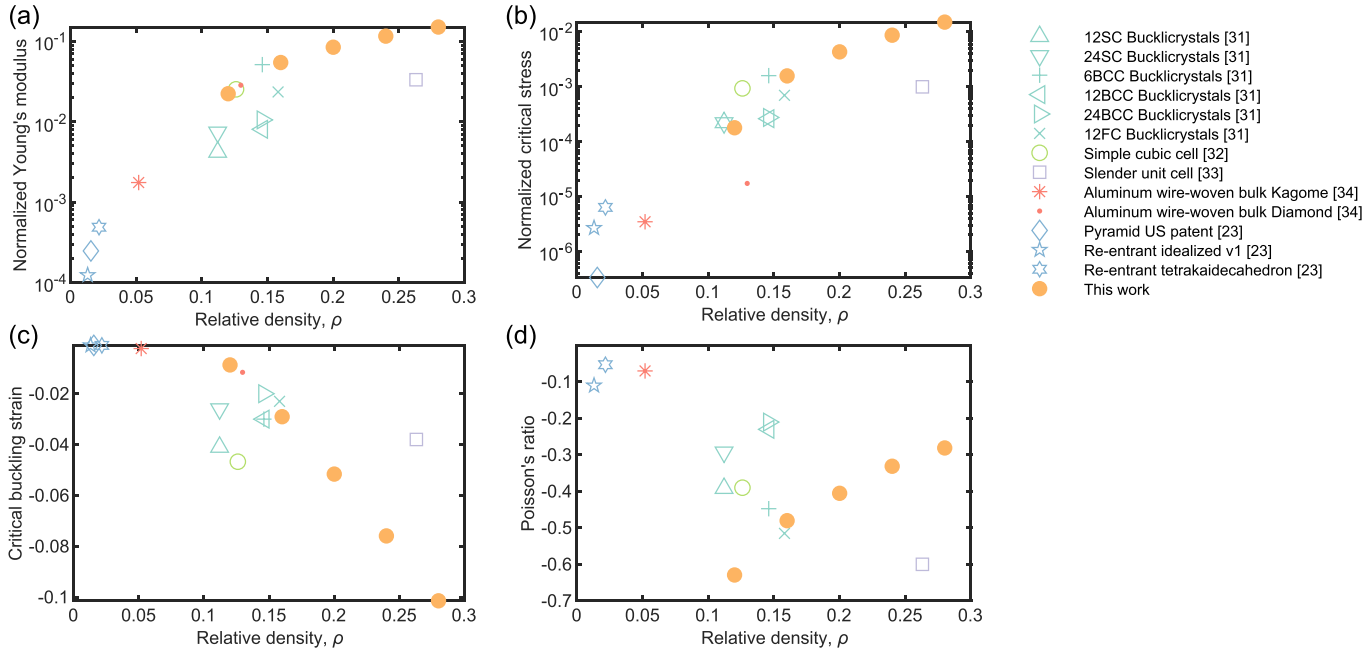

Fig. 8. Comparison of the proposed auxetic metamaterial with several typical auxetic metamaterials. (a) Normalized Young's modulus, (b) Normalized critical buckling stress, (c) Normalized critical strain, and (d) Poisson's ratio.

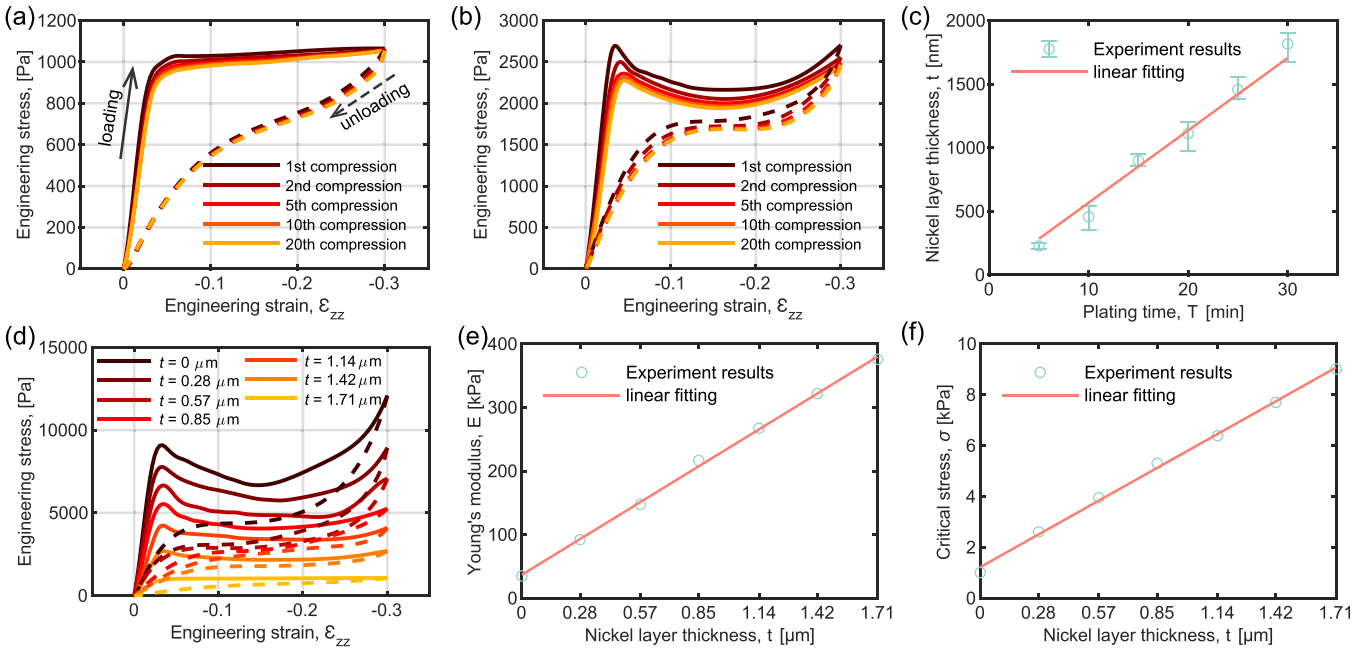

Fig. 9. Influence of nickel layer thickness on mechanical and conduction properties. Stress-strain curves of (a) a 3D-printed specimen with $\rho = 0.16$ and (b) a nickel-coated specimen with $\rho = 0.16$ and $t = 0.57$ μm from multiple compression tests. (c) Evaluation of the nickel layer thickness that is linearly dependent on plating time. (d) Stress-strain curves of nickel-coated specimens with different thicknesses of nickel layers from the first cycle of compression tests. Dependence of (e) the Young's modulus and (f) critical buckling stress on the nickel layer thickness. In the stress-strain curves, solid lines represent loading and dot lines represent unloading.

restored to its original point, in pace with the recovery of the specimen. The results further prove the remarkable resilience and stability of these specimens under multiple large compressions.

We also explored the influence of the nickel layers on the electrical conductivities by coating different thicknesses of the nickel layers on the 3D-printed specimens with $\rho = 0.16$. Fig. 10b presents the conductivity-strain curves of these specimens from the first cycle of compression tests. Analogous to the stress-strain curves in Fig. 9d, each of these conductivity-strain curves consist of three parts during loading: a steep incline followed by a drop and a gradual rise. As expected, the conduction is enhanced remarkably by plating thicker nickel layers; for example, when the thickness increases from 0.28 μm to 1.71 μm, the conductivities increase from approximately 58 S/m to 371 S/m at the initial shape (Fig. 10c).

3.4. Data maps of mechanical and conduction properties

We further conducted a more comprehensive study by investigating the mechanical and conduction properties of the material dependent on the relative density and nickel layer thickness. We fabricated a range of specimens by electroless plating of nickel layers with different thicknesses on 3D printed models with $\rho = 0.12 - 0.28$. Their effective mechanical and conduction properties, including Young's moduli, Poisson's ratios, critical buckling strains, critical buckling stresses, and electrical conductivities, were calculated from the first cycle of uniaxial compression tests. These results are presented as contour maps in Fig. 11, thus providing a method to tune the mechanical and conduction properties.

Figs. 11a and b respectively present the Young's moduli and critical stresses from the experimental results, which are normalized by the Young's modulus of the 3D-printed resin, $E_0 = 0.6615$ MPa. Increasing either the relative density or the nickel layer thickness can tremendously enhance the Young's moduli and critical stresses. After plating a 1.71 μm thick nickel layer on the 3D-printed specimen with $\rho = 0.28$, the normalized Young's modulus increases from 0.02 to 1.02 and the critical stress increases from 1.79×10^{-4} to 8.60×10^{-2} compared with the green 3D-printed specimen with $\rho = 0.12$.

Regarding the tuning of the Poisson's ratios for ν_{xy} (data were taken from the points at $\varepsilon_{zz} = -0.3$) and critical buckling strains, changing

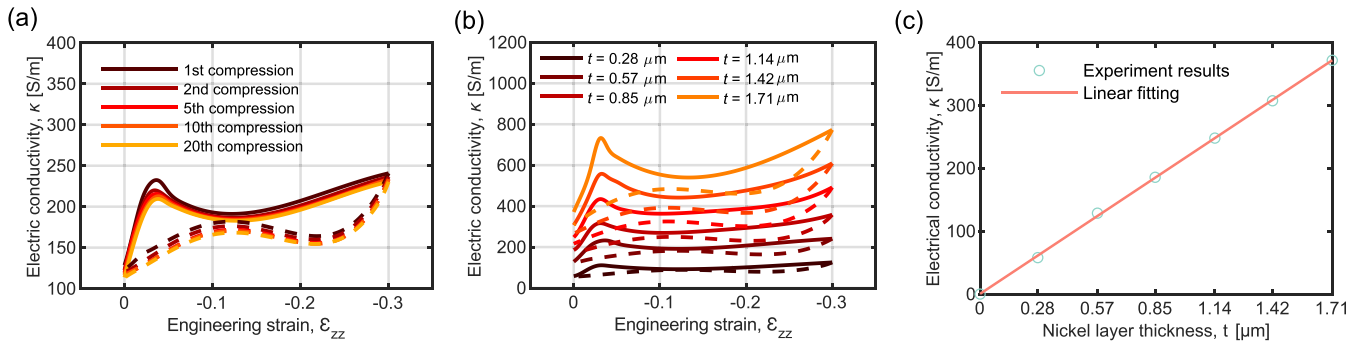

Fig. 10. Influence of nickel layer thickness on conduction properties. (a) Conductivity-strain curves of the nickel-coated specimen with $\rho = 0.16$ and $t = 0.57$ μm from multiple compression tests. (b) Conductivity-strain curves of nickel-coated specimens with different thicknesses of nickel layers from the first cycle of compression tests. (c) Dependence of conductivity on the nickel layer thickness at the initial shapes. In the conductivity-strain curves, solid lines represent loading and dot lines represent unloading.

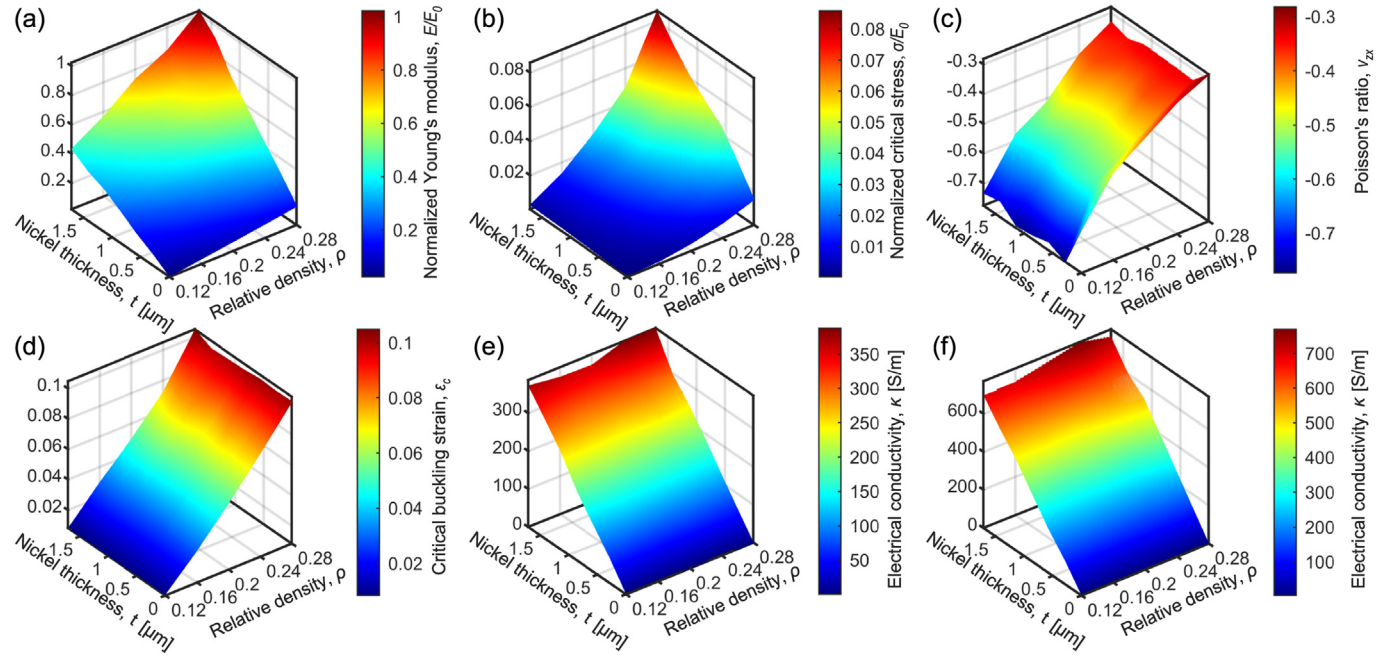

Fig. 11. 3D Contour maps of mechanical and conduction properties, including (a) normalized Young's modulus E/E_0, (b) normalized critical buckling stresses σ_c/E_0, (c) minimum Poisson's ratios ν_{zx} at $\varepsilon_{zz} = -0.3$, (d) critical buckling strains ε_c, (e) electrical conductivities κ at the initial shapes, and (f) electrical conductivities κ at critical buckling shapes. The results are built by integration of the results obtained by plating $t = 0.28$,0.57,0.85,1.14,1.42, and 1.71 μm nickel layers onto the 3D printed specimens with $\rho = 0.12$,0.16,0.20,0.24, and 0.28, as indicated by the gray dots in the first map.

only the relative densities appears to be a suitable solution (Figs. 11c and d). It is worth noting that the Poisson's ratios and critical buckling strains are nearly independent of the nickel layer thicknesses, but are dominated by the relative densities. The Poisson's ratios increase from approximately −0.78 to −0.29 and the critical buckling strains increase from 0.01 to 0.1 when the relative densities increase from 0.12 to 0.28.

However, the electrical conductivities are hugely determined by the nickel layer thicknesses. Figs. 11e and f show the electrical conductivities at the initial and critical buckling shapes, respectively. This shows that the 3D-printed specimens become conductive after plating with nickel layers of hundreds of nanometers thickness on the surfaces, and a 1.71 μm nickel layer achieves a conductivity of 700 S/m. Moreover, these results also indicate that the conductivities are difficult to manipulate by varying the relative density; although, for the same nickel layer thickness, the 3D-printed specimen with a higher relative density has a larger conductivity than the one with a lower relative density at critical buckling shapes.

4. Conclusions

We presented a novel auxetic metamaterial originating from a type of TPMS structure. The mathematically defined modeling method enables the designing of more complicated systems using the metamaterial as basic unit cells. The relative density of the metamaterial is determined by varying the level-set parameter of implicit expression. The compression tests, along with the FEM simulations, demonstrate that the auxetic behavior of the new metamaterial is dominated by buckling instability and is retained over a broad range of longitudinal strain values up to 0.3. The metamaterial was 3D printed using a rubber-like material, followed by plating with nickel nanolayers; this produces a fully reversible and resilient substrate, whose mechanical and conduction properties are highly tunable by varying the relative density and nickel layer thickness. More importantly, data maps of the Young's moduli, critical buckling stresses and strains, Poisson's ratios, and conductivities provide guidance for functional applications of the material. Finally, although this work focused only on a single TPMS structure and a single plated metal, it is highly recommended that a structural gallery combining other TPMSs and electroless plating techniques (e.g., Cu, Ag, and Au) be developed in future work, thereby paving a way towards functional applications, such as strain sensors, actuators, and electrochemical energy storage and conversion.

Declaration of Competing Interest

The authors declare that they have no known competing financial interests or personal relationships that could have appeared to influence the work reported in this paper.

References

[1] G.N. Greaves, A. Greer, R.S. Lakes, T. Rouxel, Poisson's ratio and modern materials, Nat. Mater. 10 (11) (2011) 823–837.
[2] R.S. Lakes, Negative-poisson's-ratio materials: Auxetic solids, Annu. Rev. Mater. Res. 47 (2017) 63–81.
[3] Z. Wang, C. Luan, G. Liaom, J. Liu, X. Yao, J. Fu, Progress in auxetic mechanical metamaterials: structures, characteristics, manufacturing methods and applications, Adv. Eng. Mater. 22 (10) (2020) 2000312.
[4] X. Yu, J. Zhou, H. Liang, Z. Jiang, L. Wu, Mechanical metamaterials associated with stiffness, rigidity and compressibility: a brief review, Prog. Mater. Sci. 94 (2018) 114–173.
[5] H.W. Kim, T.Y. Kim, H.K. Park, I. You, J. Kwak, J.C. Kim, H. Hwang, H.S. Kim, U. Jeong, Hygroscopic auxetic on-skin sensors for easy-to-handle repeated daily use, ACS Appl. Mater. Interfaces 10 (46) (2018) 40141–40148.
[6] Y. Jiang, Z. Liu, N. Matsuhisa, D. Qi, W.R. Leow, H. Yang, J. Yu, G. Chen, Y. Liu, C. Wan, et al., Auxetic mechanical metamaterials to enhance sensitivity of stretchable strain sensors, Adv. Mater. 30 (12) (2018) 1706589.
[7] J.I. Lipton, R. MacCurdy, Z. Manchester, L. Chin, D. Cellucci, D. Rus, Handedness in shearing auxetics creates rigid and compliant structures, Science 360 (6389) (2018) 632–635.
[8] M. Lei, W. Hong, Z. Zhao, C. Hamel, M. Chen, H. Lu, H.J. Qi, 3d printing of auxetic metamaterials with digitally reprogrammable shape, ACS Appl. Mater. Interfaces 11 (25) (2019) 22768–22776.
[9] H.M. Kolken, S. Janbaz, S.M. Leeflang, K. Lietaert, H.H. Weinans, A.A. Zadpoor, Rationally designed meta-implants: a combination of auxetic and conventional meta-biomaterials, Mater. Horiz. 5 (1) (2018) 28–35.
[10] W. Wu, X. Song, J. Liang, R. Xia, G. Qian, D. Fang, Mechanical properties of anti-tetrachiral auxetic stents, Compos. Struct. 185 (2018) 381–392.

[11] Z. Wang, A. Zulifqar, H. Hu, Auxetic composites in aerospace engineering, Advanced Composite Materials for Aerospace Engineering, Elsevier 2016, pp. 213–240.
[12] A. Airoldi, P. Bettini, P. Panichelli, M.F. Oktem, G. Sala, Chiral topologies for composite morphing structures–part i: development of a chiral rib for deformable airfoils, Bhys. Status Solidi B 252 (7) (2015) 1435–1445.
[13] B. Dyatkin, Energy focus: structural water plays key role in hybrid energy-storage device, MRS Bull. 43 (8) (2018) 567–568.
[14] P. Chang, H. Mei, Y. Tan, Y. Zhao, W. Huang, L. Cheng, A 3d-printed stretchable structural supercapacitor with active stretchability/flexibility and remarkable volumetric capacitance, J. Mater. Chem. A 8 (27) (2020) 13646–13658.
[15] L. Weng, J. Zhou, R. Cai, Analytical model of li-ion diffusion-induced stress in nanowire and negative poisson's ratio electrode under different operations, Int. J. Mech. Sci. 141 (2018) 245–261.
[16] H. Yasuda, J. Yang, Reentrant origami-based metamaterials with negative poisson's ratio and bistability, Phys. Rev. Lett. 114 (18) (2015) 185502.
[17] Z. Chen, X. Wu, Y.M. Xie, Z. Wang, S. Zhou, Re-entrant auxetic lattices with enhanced stiffness: a numerical study, Int. J. Mech. Sci. 178 (2020) 105619.
[18] X. Li, Z. Lu, Z. Yang, C. Yang, Directions dependence of the elastic properties of a 3d augmented re-entrant cellular structure, Mater. Des. 134 (2017) 151–162.
[19] X.-T. Wang, B. Wang, X.-W. Li, L. Ma, Mechanical properties of 3d re-entrant auxetic cellular structures, Int. J. Mech. Sci. 131 (2017) 396–407.
[20] Q. Gao, L. Wang, Z. Zhou, Z. Ma, C. Wang, Y. Wang, Theoretical, numerical and experimental analysis of three-dimensional double-v honeycomb, Mater. Des. 139 (2018) 380–391.
[21] Q. Gao, C.A. Tan, G. Hulbert, L. Wang, Geometrically nonlinear mechanical properties of auxetic double-v microstructures with negative poisson's ratio, Eur. J. Mech.-A/Solids 80 (2020) 103933.
[22] Q. Gao, X. Zhao, C. Wang, L. Wang, Z. Ma, Crashworthiness analysis of a cylindrical auxetic structure under axial impact loading, Sci. China Technol. Sci. 63 (1) (2020) 140–154.
[23] J.C.Á. Elipe, A.D. Lantada, Comparative study of auxetic geometries by means of computer-aided design and engineering, Smart Mater. Struct. 21 (10) (2012) 105004.
[24] Y. Jiang, Y. Li, 3d printed chiral cellular solids with amplified auxetic effects due to elevated internal rotation, Adv. Eng. Mater. 19 (2) (2017) 1600609.
[25] L. Mizzi, E. Mahdi, K. Titov, R. Gatt, D. Attard, K.E. Evans, J.N. Grima, J.-C. Tan, Mechanical metamaterials with star-shaped pores exhibiting negative and zero poisson's ratio, Mater. Des. 146 (2018) 28–37.
[26] H. Ebrahimi, D. Mousanezhad, H. Nayeb-Hashemi, J. Norato, A. Vaziri, 3d cellular metamaterials with planar anti-chiral topology, Mater. Des. 145 (2018) 226–231.
[27] M. Fu, F. Liu, L. Hu, A novel category of 3d chiral material with negative poisson's ratio, Compos. Sci. Technol. 160 (2018) 111–118.
[28] Z. Lu, Q. Wang, X. Li, Z. Yang, Elastic properties of two novel auxetic 3d cellular structures, Int. J. Solids Struct. 124 (2017) 46–56.
[29] H. Seifi, A.R. Javan, A. Ghaedizadeh, J. Shen, S. Xu, Y.M. Xie, Design of hierarchical structures for synchronized deformations, Sci. Rep. 7 (1) (2017) 1–7.
[30] J.T. Overvelde, S. Shan, K. Bertoldi, Compaction through buckling in 2d periodic, soft and porous structures: effect of pore shape, Adv. Mater. 24 (17) (2012) 2337–2342.
[31] S. Babaee, J. Shim, J.C. Weaver, E.R. Chen, N. Patel, K. Bertoldi, 3d soft metamaterials with negative poisson's ratio, Adv. Mater. 25 (36) (2013) 5044–5049.
[32] J. Shen, S. Zhou, X. Huang, Y.M. Xie, Simple cubic three-dimensional auxetic metamaterials, Phys. Status Solidi B 251 (8) (2014) 1515–1522.
[33] X. Ren, J. Shen, P. Tran, T.D. Ngo, Y.M. Xie, Design and characterisation of a tuneable 3d buckling-induced auxetic metamaterial, Mater. Des. 139 (2018) 336–342.
[34] S.C. Han, D.S. Kang, K. Kang, Two nature-mimicking auxetic materials with potential for high energy absorption, Mater. Today 26 (2019) 30–39.
[35] J. Zeng, H. Hu, L. Zhou, A study on negative poissons ratio effect of 3d auxetic orthogonal textile composites under compression, Smart Mater. Struct. 26 (6) (2017), 065014, .
[36] L. Zhou, L. Jiang, H. Hu, Auxetic composites made of 3d textile structure and polyurethane foam, Phys. Status Solidi B 253 (7) (2016) 1331–1341.
[37] G.W. Milton, Composite materials with poisson's ratios close to1, J. Mech. Phys. Solids 40 (5) (1992) 1105–1137.
[38] O. Al-Ketan, R.K. Abu Al-Rub, Multifunctional mechanical metamaterials based on triply periodic minimal surface lattices, Adv. Eng. Mater. 21 (10) (2019) 1900524.
[39] L. Han, S. Che, An overview of materials with triply periodic minimal surfaces and related geometry: from biological structures to self-assembled systems, Adv. Mater. 30 (17) (2018) 1705708.
[40] X. Guo, X. Zheng, Y. Yang, X. Yang, Y. Yi, Mechanical behavior of tpms-based scaffolds: a comparison between minimal surfaces and their lattice structures, SN Appl. Sci. 1 (10) (2019) 1145.
[41] X. Zheng, X. Guo, Y. Yang, Z. Fu, K. Du, C. Wang, Y. Yi, Structure-dependent analysis of nanoporous metals: clues from mechanical, conduction, and flow properties, J. Phys. Chem. C 122 (29) (2018) 16803–16809.
[42] D.W. Abueidda, M. Bakir, R.K.A. Al-Rub, J.S. Bergström, N.A. Sobh, I. Jasiuk, Mechanical properties of 3d printed polymeric cellular materials with triply periodic minimal surface architectures, Mater. Des. 122 (2017) 255–267.
[43] F. Liu, Z. Mao, P. Zhang, D.Z. Zhang, J. Jiang, Z. Ma, Functionally graded porous scaffolds in multiple patterns: new design method, physical and mechanical properties, Mater. Des. 160 (2018) 849–860.
[44] N. Yang, Z. Quan, D. Zhang, Y. Tian, Multi-morphology transition hybridization cad design of minimal surface porous structures for use in tissue engineering, Comput. Aided Des. 56 (2014) 11–21.
[45] D.-J. Yoo, K.-H. Kim, An advanced multi-morphology porous scaffold design method using volumetric distance field and beta growth function, Int. J. Precis. Eng. Manuf. 16 (9) (2015) 2021–2032.
[46] X. Zheng, Z. Fu, K. Du, C. Wang, Y. Yi, Minimal surface designs for porous materials: from microstructures to mechanical properties, J. Mater. Sci. 53 (14) (2018) 10194–10208.
[47] C. Soyarslan, V. Blümer, S. Bargmann, Tunable auxeticity and elastomechanical symmetry in a class of very low density core-shell cubic crystals, Acta Mater. 177 (2019) 280–292.
[48] L.C. Felix, C.F. Woellner, D.S. Galvao, Mechanical and energy-absorption properties of schwarzites, Carbon 157 (2020) 670–680.
[49] R. Hamzehei, J. Kadkhodapour, A.P. Anaraki, S. Rezaei, S. Dariushi, A.M. Rezadoust, Octagonal auxetic metamaterials with hyperelastic properties for large compressive deformation, Int. J. Mech. Sci. 145 (2018) 96–105.
[50] S. Yuan, F. Shen, J. Bai, C.K. Chua, J. Wei, K. Zhou, 3d soft auxetic lattice structures fabricated by selective laser sintering: Tpu powder evaluation and process optimization, Mater. Des. 120 (2017) 317–327.
[51] Q. Cheng, Y. Liu, J. Lyu, Q. Lu, X. Zhang, W. Song, 3d printing-directed auxetic kevlar aerogel architectures with multiple functionalization options, J. Mater. Chem. A 8 (28) (2020) 14243–14253.
[52] L. Yang, O. Harrysson, H. West, D. Cormier, Compressive properties of ti–6al–4v auxetic mesh structures made by electron beam melting, Acta Mater. 60 (8) (2012) 3370–3379.
[53] L. Yang, O. Harrysson, H. West, D. Cormier, Mechanical properties of 3d re-entrant honeycomb auxetic structures realized via additive manufacturing, Int. J. Solids Struct. 69 (2015) 475–490.
[54] K.-J. Kang, Wire-woven cellular metals: the present and future, Prog. Mater. Sci. 69 (2015) 213–307.
[55] A.H. Schoen, Infinite periodic minimal surfaces without self-intersections, Technical Note D-5541, Nation. Aero. Space Admin.1970.
[56] H.A. Schwarz, Gesammelte Mathematische Abhandlungen, vol. 260, American Mathematical Soc., 1972
[57] I. Watanabe, A. Yamanaka, Voxel coarsening approach on image-based finite element modeling of representative volume element, Int. J. Mech. Sci. 150 (2019) 314–321.
[58] I. Watanabe, D. Setoyama, N. Nagasako, N. Iwata, K. Nakanishi, Multiscale prediction of mechanical behavior of ferrite–pearlite steel with numerical material testing, Int. J. Numer. Methods Eng. 89 (7) (2012) 829–845.